

Functional in situ assessment of human articular cartilage using MRI: a whole-knee joint loading device

Sven Nebelung¹ · Manuel Post¹ · Stefan Raith² · Horst Fischer² ·
Matthias Knobe³ · Benedikt Braun⁴ · Andreas Prescher⁵ · Markus Tingart⁶ ·
Johannes Thüring¹ · Philipp Bruners¹ · Holger Jahr⁶ · Christiane Kuhl¹ ·
Daniel Truhn¹

Received: 30 November 2016 / Accepted: 23 June 2017 / Published online: 6 July 2017
© Springer-Verlag GmbH Germany 2017

Abstract The response to loading of human articular cartilage as assessed by magnetic resonance imaging (MRI) remains to be defined in relation to histology and biomechanics. Therefore, an MRI-compatible whole-knee joint loading device for the functional in situ assessment of cartilage was developed and validated in this study. A formalin-fixed human knee was scanned by computed tomography in its native configuration and digitally processed to create femoral and tibial bone models. The bone models were covered by artificial femoral and tibial articular cartilage layers in their native configuration using cartilage-mimicking polyvinyl siloxane. A standardized defect of 8 mm diameter was created within the artificial cartilage layer at the central medial femoral condyle, into which native cartilage samples of similar dimensions were placed. After describing its design and specifications, the comprehensive validation of

the device was performed using a hydraulic force gauge and digital electronic pressure-sensitive sensors. Displacement-controlled quasi-static uniaxial loading to 2.5 mm ($\delta_{2.5}$) and 5.0 mm ($\delta_{5.0}$) of the mobile tibia versus the immobile femur resulted in forces of 141 ± 8 N ($\delta_{2.5}$) and 906 ± 38 N ($\delta_{5.0}$) (on the entire joint) and local pressures of 0.680 ± 0.088 MPa ($\delta_{2.5}$) and 1.050 ± 0.100 MPa ($\delta_{5.0}$) (at the site of the cartilage sample). Upon confirming the MRI compatibility of the set-up, the response to loading of macroscopically intact human articular cartilage samples ($n = 5$) was assessed on a clinical 3.0-T MR imaging system using clinical standard proton-density turbo-spin echo sequences and T2-weighted multi-spin echo sequences. Serial imaging was performed at the unloaded state (δ_0) and at consecutive loading positions (i.e. at $\delta_{2.5}$ and $\delta_{5.0}$). Biomechanical unconfined compression testing (Young's modulus) and histological assessment (Mankin score) served as the standards of reference. All samples were histologically intact (Mankin score, 1.8 ± 1.3) and biomechanically reasonably homogeneous (Young's modulus, 0.42 ± 0.14 MPa). They could be visualized in their entirety by MRI and significant decreases in sample height [δ_0 : 2.86 ± 0.25 mm; $\delta_{2.5}$: 2.56 ± 0.25 mm; $\delta_{5.0}$: 2.02 ± 0.16 mm; $p < 0.001$ (repeated-measures ANOVA)] as well as pronounced T2 signal decay indicative of tissue pressurization were found as a function of compressive loading. In conclusion, our compression device has been validated for the noninvasive response-to-loading assessment of human articular cartilage by MRI in a close-to-physiological experimental setting. Thus, in a basic research context cartilage may be functionally evaluated beyond mere static analysis and in reference to histology and biomechanics.

✉ Sven Nebelung
snebelung@ukaachen.de

¹ Department of Diagnostic and Interventional Radiology, Aachen University Hospital, Pauwelsstrasse 30, 52074 Aachen, Germany

² Department of Dental Materials and Biomaterials Research, Aachen University Hospital, Aachen, Germany

³ Department of Orthopaedic Trauma, Aachen University Hospital, Aachen, Germany

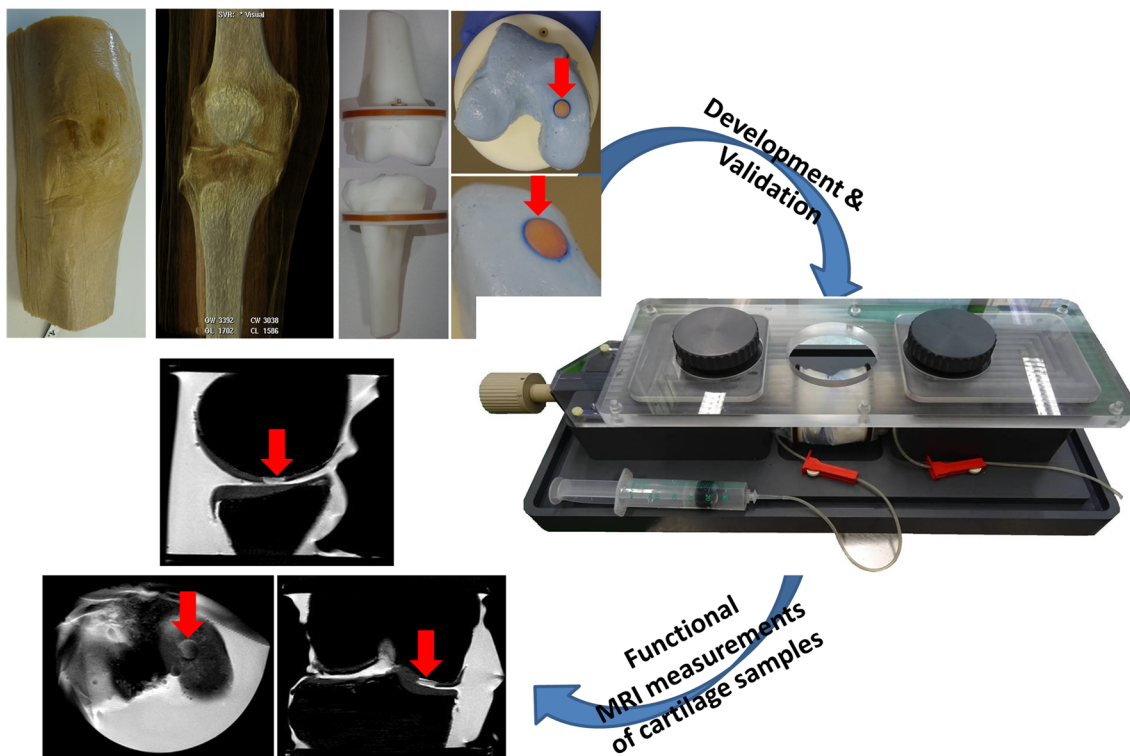
⁴ Department of Trauma, Hand and Reconstructive Surgery, Saarland University Hospital, Homburg, Germany

⁵ Institute of Molecular and Cellular Anatomy, Aachen University Hospital, Aachen, Germany

⁶ Department of Orthopaedics, Aachen University Hospital, Aachen, Germany

Graphical Abstract

A whole-knee joint loading device for the functional assessment of human articular cartilage



Keywords Cartilage · Artificial knee joint · Functional assessment · MRI · Loading device

1 Introduction

Cartilage degeneration needs to be reliably detected at its earliest stages, as long as the pathology is still potentially reversible and preventive interventions such as axis-modifying surgery or pharmacotherapy are successful (Bay-Jensen et al. 2010). However, early cartilage degenerative changes cannot be properly evaluated by currently available clinical routine imaging modalities such as conventional radiography, computer tomography or morphological MRI (Guermazi et al. 2015; Link et al. 2016; Palmer et al. 2013).

Cartilage degeneration is currently theorized to be the result of an unfavourable biomechanical environment and susceptible cartilage tissue (Johnson et al. 2012). Biomechanically, ‘joint level factors’ such as malalignment, abnormal loading (e.g. due to altered gait) and injury may contribute, while individual factors like age, sex, genetics, ethnicity, diet and obesity also affect the tissue’s biomechanical properties (Johnson et al. 2012). As long as normal locomotion, cartilage biology and structural integrity of the joint are maintained, cartilage homeostasis is balanced, and

the tissue is healthy (Andriacchi et al. 2009). However, once loading stresses overwhelm the tissue’s capacity to withstand loading, the cascade of degenerative changes is initiated. Such early degenerative changes include loss of proteoglycans, disruption of collagen fibre orientation and increase in water content (‘cartilage oedema’) alongside altered biomechanical properties (Kleemann et al. 2005; Madry et al. 2016; Palmer et al. 2013). Common consensus prevails that biochemical, compositional and biomechanical changes are closely associated (Temple-Wong 2009). Therefore, recent diagnostic approaches aimed at detecting early-stage cartilage degeneration tried to evaluate the tissue’s functionality. In this regard, MRI is the imaging modality of choice due to its excellent soft tissue contrast and lack of ionizing radiation. Functional assessment by use of MRI assessed the articular cartilage’s response to loading which has so far been studied in samples (Juras et al. 2009; Nebelung et al. 2017; Xia et al. 2011), cadaver joints (Chan et al. 2009; Herberhold et al. 1999; Shiomi et al. 2010) and patients (Chan et al. 2016; Souza et al. 2014; Wang et al. 2015), both in health and in disease. Although principal differences in the experimental set-up and protocols limited comparability, the studies above nonetheless indicated that the loading response of diseased cartilage is abnormal and indicative of cartilage pathology.

Loading characteristics within a joint (e.g. knee joint) vary considerably as a function of weight, alignment, ligament stability, joint site as well as cartilage and meniscus status (Agneskirchner et al. 2007; Lee et al. 2006). Therefore, in an experimental context, whole-joint configurations are a prerequisite for close-to-physiological loading of cartilage. Previous experimental studies assessing the cartilage response to loading in a whole-joint configuration (Chan et al. 2009; Herberhold et al. 1999; Shiomi et al. 2010) have not referenced MRI data to alternative measures of cartilage quality assessment such as histology or biomechanics. Histology, however, is commonly considered the gold standard reference. Thus, a true need exists for a set-up that allows functional imaging of human articular cartilage in a whole-joint ex vivo loading model under standardized conditions with reference to histological and biomechanical evaluation.

Thus, the purpose of our study was (1) to develop and validate an MRI-compatible whole-knee joint in situ compressive loading device; (2) to noninvasively assess the response to loading of intact human articular cartilage samples within this device by MRI and (3) to correlate these findings to conventional histological and biomechanical measures. Our hypotheses were that (1) the compressive loading device can deliver quasi-static compressive loading to articular cartilage samples in a consistent, standardized and reproducible manner; that (2) loading-induced changes can be reliably detected by clinical standard MRI sequences; and that (3) these changes can be correlated with histological and biomechanical reference measures.

2 Materials and methods

2.1 Study design

This study consisted of two parts: 1, the development and validation of a whole-knee joint compressive loading device and 2, the prospective comparative in situ and ex vivo imaging study using the device for standardized compression of surgically obtained human femoral knee joint cartilage samples. The cartilage samples were obtained from patients undergoing total knee replacement. Accordingly, local institutional review board approval on the use of cartilage samples (Ethical Committee, RWTH Aachen University, Germany, AZ-EK157/13) and individual written informed patient consent were obtained beforehand.

2.2 Compressive loading device

2.2.1 Preparatory work

An intact, thoroughly formalin-fixed (10% neutral buffered formalin) right knee was obtained from the Department of

Anatomy at RWTH Aachen University (female donor, 67 years, deceased due to unrelated reasons) (Fig. 1a). The lower and upper thirds of the femur and tibia, respectively, were preserved. The entire knee was scanned in its native configuration using multidetector-row computed tomography (SOMATOM Definition Flash, Siemens, Erlangen, Germany). Sequential scanning was performed in the craniocaudal direction with the following scan parameters: 120 kVp tube voltage, 0.75 mm slice thickness, 16×0.75 mm slice collimation, 1500 HU window width, 450 HU window centre, 0.5 mm reconstruction increment, pitch of 1 and Siemens B60s as reconstruction kernel. A 512×512 matrix was used for subsequent sagittal and coronal image reconstructions. The field of view (158×158 mm) was adapted to the joint outline, and bone shapes of femur and tibia were acquired with a voxel size of $0.311 \times 0.311 \times 0.5$ mm. The CT scan demonstrated absence of any gross focal cartilage or bone pathologies (Fig. 1b). While preserving the native configuration of both femur and tibia in terms of axis, orientation and position, bone segmentation was performed separately using Mimics[®] software (v14.0, Materialise Inc., Leuven, Belgium) and data were exported in the standard triangulation language (STL) format.

After CT scanning, the knee joint and the periarticular regions were dissected and cleared from soft tissues except for the periosteum and the articular femoral and tibial cartilage (Fig. 1c). The native cartilage-covered tibial and femoral bones were used to create silicone moulds (Dublisil, Drevedentamid, Unna, Germany) as cartilage-holding negatives (Fig. 2a). Afterwards, the tibial and femoral bones were enzymatically macerated using a mix of amylase, lipase, papain and detergents (Simonsen et al. 2011) over a period of two days to remove all residual soft tissue and to obtain white-bone specimens (Fig. 2b). The maceration process was effective in removing all cartilage tissue, including the calcified cartilage layer adjacent to the subchondral lamella (Fig. 1d). Therefore, the white-bone specimens were re-scanned separately by CT (as above) to exactly recreate the bone surfaces. After surface segmentation and data export as triangulated surface data (as above), the digital bone models were modified by digitally adding a metaphyseal ‘collar’ for the fixation of the artificial joint capsule. To this end, a solid ring (90 mm diameter, 10 mm height, peripheral central groove with 6 mm diameter and 2 mm depth) was digitally attached to the bone models at an equidistance of 30 mm to the joint line (Fig. 1e). Then, the modified femoral and tibial bone models were fabricated using heated thermoplastic acrylonitrile butadiene styrene (ABS plus 430, Stratasys, Eden Prairie, USA) and a 3D rapid prototyping printer (Dimension SST 1200es, Stratasys) (Fig. 1f). The bone models were printed layer by layer in the fused deposition modelling technique within 20 h; the technical parameters were as follows: 0.254 mm layer thickness, 100% degree

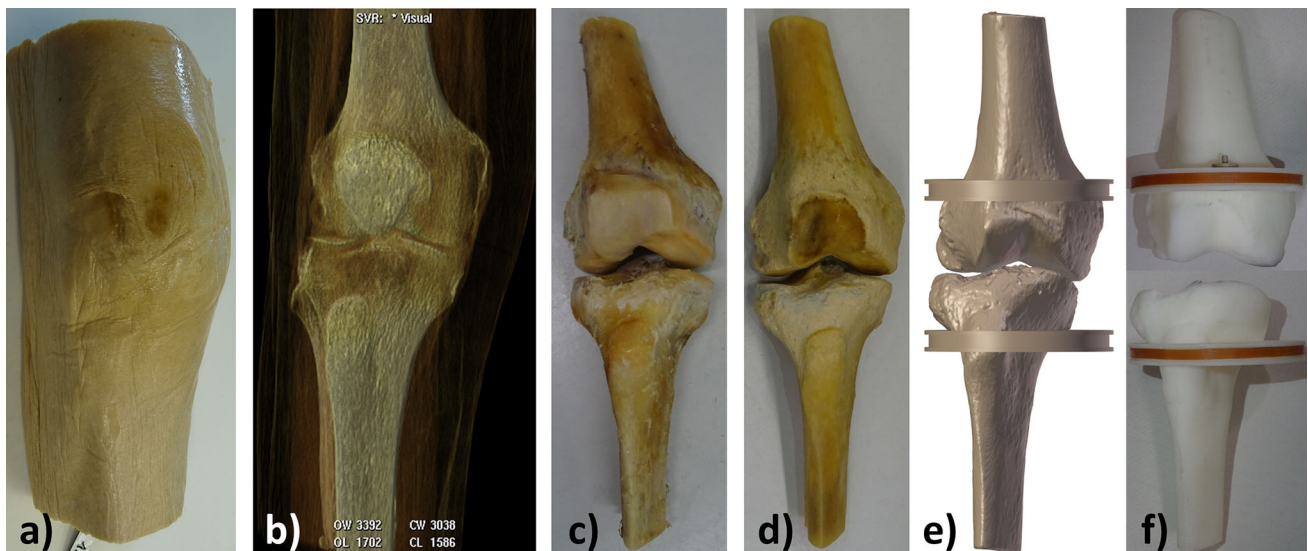


Fig. 1 **a** A right human knee joint, formalin-fixed, with surrounding soft tissues including skin. **b** Screenshot of the 3D-rendered CT scan of the native knee. The native configuration of the femur and tibia in terms of axis, orientation and position was determined and preserved for all subsequent project stages. **c, d** Femur and tibia following dissection of surrounding soft tissues prior to (**c**) and following enzymatic macera-

tion of all residual soft tissues, including the articular cartilage (**d**). **e, f** 3D renderings of the femoral (*top*) and tibial bone model (*bottom*) with grooved rings attached to the diaphysis for the fixation of the artificial joint capsule (**e**) that were used to 3D print the actual bone models (**f**)

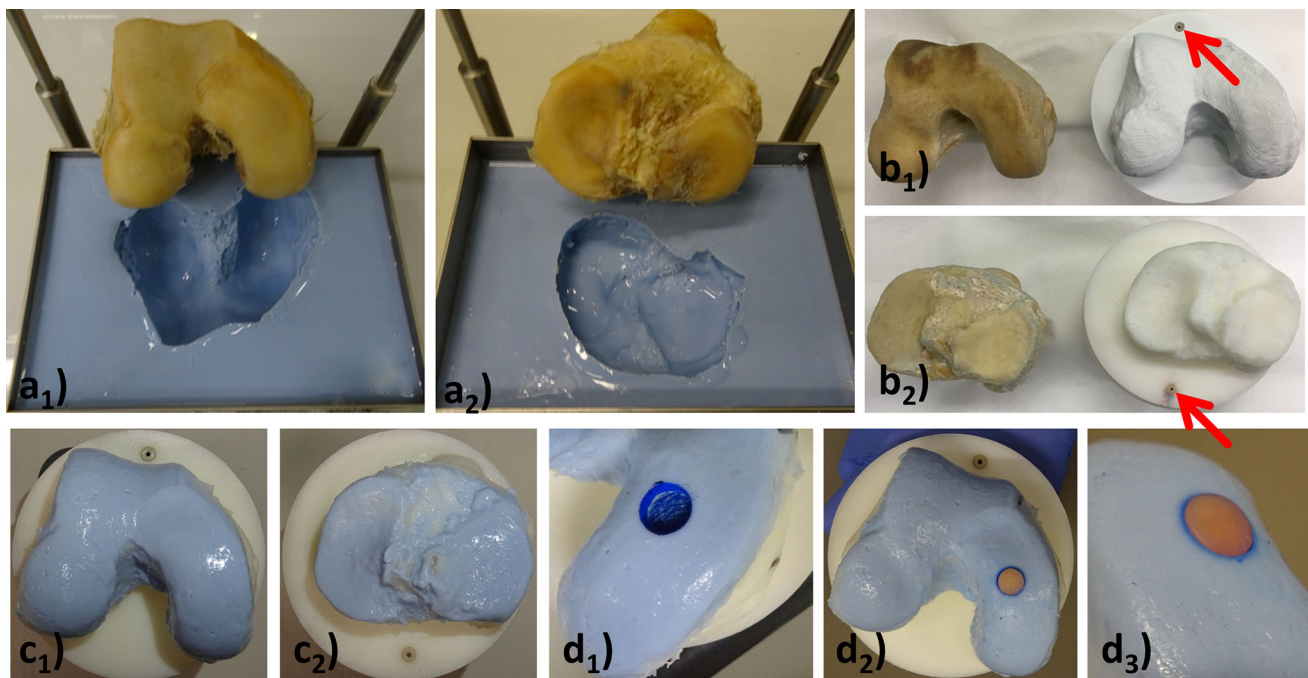


Fig. 2 **a** Silicone moulds as cartilage-holding negatives were created of the femur (**a₁**) and tibia (**a₂**) prior to enzymatic maceration. **b** The artificial bone models (*right*), i.e. cartilage-deficient positives [femur (**b₁**), tibia (**b₂**)], are displayed next to the original bones following enzymatic maceration (*left*). **c** To obtain wiroasil® silicone-coated femoral (**c₁**) and tibial (**c₂**) bone models, the cartilage-deficient positives (as displayed in **b**) were inserted into the silicone moulds (as displayed in **a**) and the resultant space (i.e. the layer of the original native articu-

lar cartilage) was replaced by wiroasil®. **d** At the central aspect of the medial femoral condyle, a standardized 8-mm-diameter circular defect was created (**d₁**) and filled with cartilage samples of equal dimensions [top view (**d₂**); side view (**d₃**)]. For in- and outflow regulation of the subsequently attached artificial joint ‘capsule’, tubular connection pins were attached to the grooved rings of the bone models (*red arrows* in **b**)

of infill. Subsequently, customized tubular connection pins (diameter: 2 mm; material: PEEK) were integrated into the solid metaphyseal ‘collars’ for regulation of in- and outflow (Fig. 2b).

To exactly recreate the artificial cartilage layer in its native topoanatomic configuration, wiroxil[®] silicone (polyvinyl siloxane) (Bego, Bremen, Germany) was used to cover the articulating surfaces of the bone models. Wiroxil[®] was identified as an appropriate cartilage-mimicking material due to its favourable MRI signal, high stiffness, mechanical stability and easy preparation (Lopez et al. 2007). Based on published data (Lopez et al. 2007), the two components (wiroxil-1:wiroxil-2) were mixed in a 0.45:0.55 mixing ratio to produce a high-stiffness excellent-bonding cartilage-mimicking layer. Once mixed, wiroxil[®] as viscous liquid cures rapidly into a rubberlike solid while taking the shape of whatever surface it is covering while curing. In our study, the 3D-printed standardized bone models (cartilage-deficient positives, Fig. 2b) were inserted into the silicone moulds (cartilage-holding negative, Fig. 2a) after filling the latter with viscous wiroxil[®]. A metallic framework adjusted to the dimensions of the bone models was used to obtain reproducible orientation and alignment while creating the wiroxil[®] coating. After a curing period of 5 min, wiroxil[®]-coated femoral and tibial bone models were obtained (cartilage-holding positives, Fig. 2c). Matching of the femoral and tibial articular cartilage layers (native knee) to the artificial wiroxil[®] layers (wiroxil[®]-coated bone models) in terms of topography and dimension was confirmed using the CT system above. Cartilage layer thickness (native and artificial) was measured at defined locations across the entire joint, i.e. at the centres of the medial and lateral femoral and tibial condyles, respectively, on sagittal and coronal sections alike. For the femur, the medial and lateral cartilage thickness (native/artificial) was found to be 2.95/3.0 and 2.0/1.9 mm, respectively, while for the tibia, the respective medial and lateral condylar cartilage thickness was determined as 2.8/3.1 and 2.8/2.8 mm, respectively.

Furthermore, as the response to loading of native cartilage was to be studied in a close-to-physiological setting, a standardized defect within the wiroxil[®] layer was created as the cartilage site-to-be. To this end, an 8-mm-diameter skin biopsy punch (pfm-medical, Cologne, Germany) was used to create an 8-mm-diameter circular defect at the centre of the medial femoral condyle (Fig. 2d₁) which was filled with cartilage sample of equal dimensions (Fig. 2d_{2,3}) as detailed below (see Sect. 2.3.1). The centre of the medial femoral condyle was chosen as the cartilage site-to-be because it is the initial point of contact as was determined in pilot studies using completely wiroxil[®]-covered bone models.

2.2.2 Description

An MRI-compatible device was constructed to hold the bone models in their native configuration in terms of axis, orientation and position and to allow for displacement-controlled, quasi-static, uniaxial compressive loading of the native cartilage samples.

To generate individualized supports for the reproducible fixation of the bone models, the specific geometries of these supports (i.e. negative shapes of two paired holding shells) were determined by Boolean operations. Thus, bone segmentation outlines were subtracted from a massive rectangular beveled PVC block [femoral side: 95 × 70 × 70 mm; tibial side: 100 × 70 × 70 mm (length × width × height); corner radius: R15] using the software package Blender[®] v2.76 (Blender Foundation, Amsterdam, Netherlands). Particular attention was paid to align the shell outlines strictly perpendicular to the joint line. The holding shells were manufactured on a five-axis universal milling machine (CNC DMU 50, DMG Mori, Leonberg, Germany) using rigid polyvinyl chloride (PVC). Upon positioning of the wiroxil[®]-coated femoral and tibial bone models in their respective holding shells, fixation was achieved by four polyether ether ketone (PEEK) screws per side (femoral side: M12x1 mm; tibial side: M10x1 mm) (Fig. 3a). The paired holding shells were dimensioned to fit exactly into their respective non-mobile PVC fixation mount (femoral side: 175 × 130 × 120 mm; tibial side: 200 × 130 × 120 mm). The fixation mounts were attached to the PVC base plate (600 × 275 × 40 mm) by a total of 12 PEEK screws (i.e. six per fixation mount) (M25x1 mm). A massive directional PVC screw (M60x1 mm) was used to secure the position of the femoral holding shells within the fixation mount. Thus, the femoral holding shells were firmly fixed and immobilized, while the tibial holding shells could be axially displaced perpendicularly to the joint line (Fig. 3b).

To create the artificial joint capsule, a transparent polyethylene video camera drape (Dahlhausen, Cologne, Germany) was cut to the appropriate size, attached to the metaphyseal ‘collars’ of the bone models and sealed by rubber O-rings. The joint capsule was filled with standard PBS buffer by use of a 50-ml perfusor syringe and standard intravenous extensions (B. Braun Medical, Melsungen, Germany) attached to the tubular connection pins as detailed above (Fig. 3c).

Details of the actuator are displayed in Fig. 4. Rotations of a PEEK screw (M22x1 mm) brought about axial forward displacement of the tibial holding shells. Screw rotations were guided by a PVC scale ring and actuated an array of PEEK and PVC components contained within a T-shaped PVC casting. The actuator consisted of PEEK and PVC components exclusively, as prolonged quasi-static compressive loading was to be upheld. Viscoelastic foam materials as used in similar applications tend to display considerable

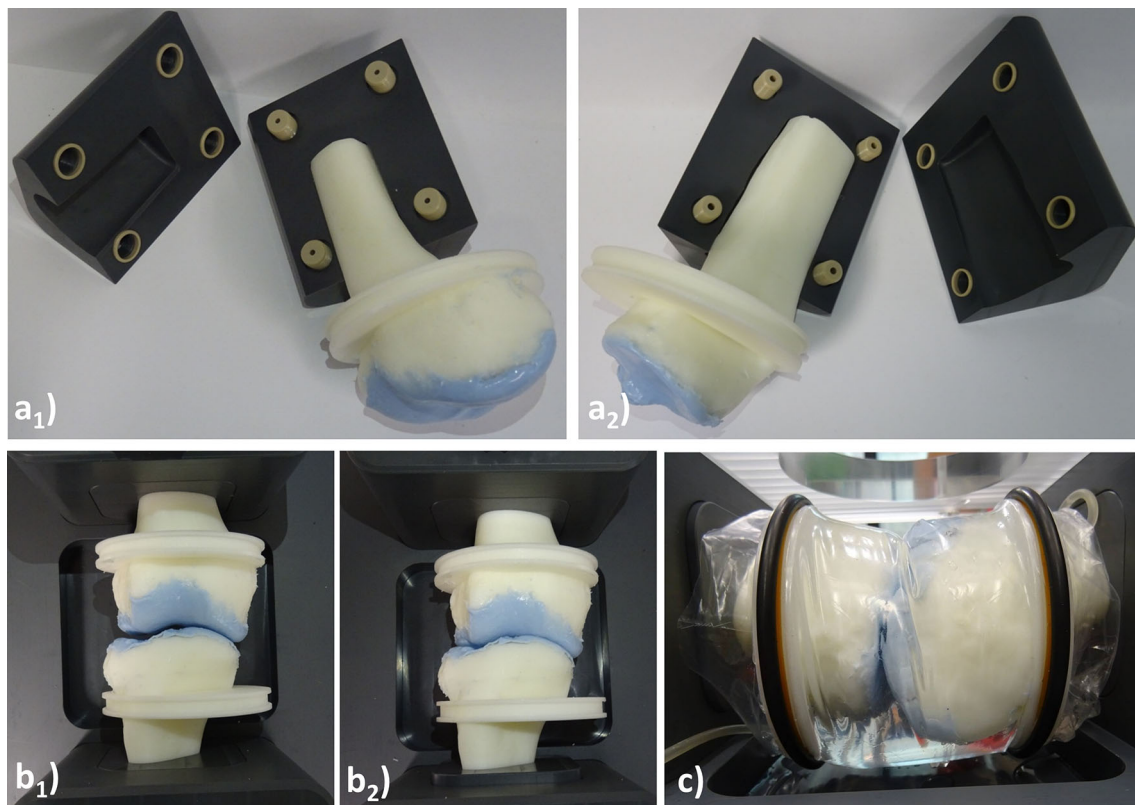


Fig. 3 **a** Wirosil[®]-coated bone models in their PVC holding shells, which were fixed by four PEEK screws per side [femoral side (**a**₁); tibial side (**a**₂)]. **b** The paired holding shells were fitted into the non-mobile PVC component attached to the PVC base plate. The tibial component (*bottom*) was axially displaced perpendicularly to the joint line, while the femoral component (*top*) was firmly fixed. The unloaded displace-

ment position (δ_0) (**b**₁) and the 5 mm displacement position ($\delta_{5.0}$) (**b**₂) are displayed. **c** The artificial joint capsule was created by attaching a transparent polyethylene tube to the bone model rings, sealing with rubber O-rings and subsequent filling with PBS buffer (femur right and tibia left)

stress relaxation (Shiomi et al. 2010), which we wanted to avoid. A demountable transparent polymethylmethacrylate cover plate was fitted onto the non-mobile fixation mounts' top surfaces to compensate for any bending forces present at loading (Fig. 5a). The entire compressive loading device was placed centrally within the MRI bore and on the patient bed with the leg axis of the knee model aligned along the static magnetic field b_0 (Fig. 5b).

2.2.3 Validation

Actuation of loading was validated using a digital hydraulic force gauge (#HKMD29D, Induk, Wuppertal, Germany) with the following specifications: 0–2.5 kN pressure range $\pm 1.0\%$ (of full scale) accuracy. A copy of the femoral bone model was digitally modified using Blender software as above to remove the femoral shaft from the femoral condyles to create a femoral condyles-only bone model, which was 3D-printed and covered with wirosil[®] as above. In keeping the overall configuration of the experimental set-up, the load cell of the force gauge was positioned between the femoral hold-

ing shells and the modified femoral bone model and used to determine resultant total knee loads at target axial displacements of 2.5 mm ($\delta_{2.5}$) and 5 mm ($\delta_{5.0}$). Axial displacement was induced by 2.5 and 5 full rotations of the actuating screw. In total, five consecutive measurements, each 30 minutes apart to allow for adequate relaxation of the wirosil[®], were performed and the resultant forces were determined as 141 ± 8 N ($\delta_{2.5}$) and 906 ± 38 N ($\delta_{5.0}$). The coefficient of variation [calculated as $(SD/M) * 100$] was calculated as 5.7 and 4.2%, respectively.

The tibiofemoral pressure levels during loading were determined using digital electronic pressure-sensitive sensors (K-Scan 4000, 10.000 psi, Tekscan, Boston, MA, USA). This system has been widely used for static and dynamic force and pressure mapping in the human knee joint (Agneskirchner et al. 2007; Suero et al. 2015). The pressure-sensitive area of the sensor contains 62 sensor elements/cm², has a thickness of 0.1 mm and measures a maximum pressure of 68.950 kPa at a spatial resolution of 0.83 mm. As it is flexible and thin, the sensor area conforms well to the specific anatomy of the medial and lateral joint compartments.

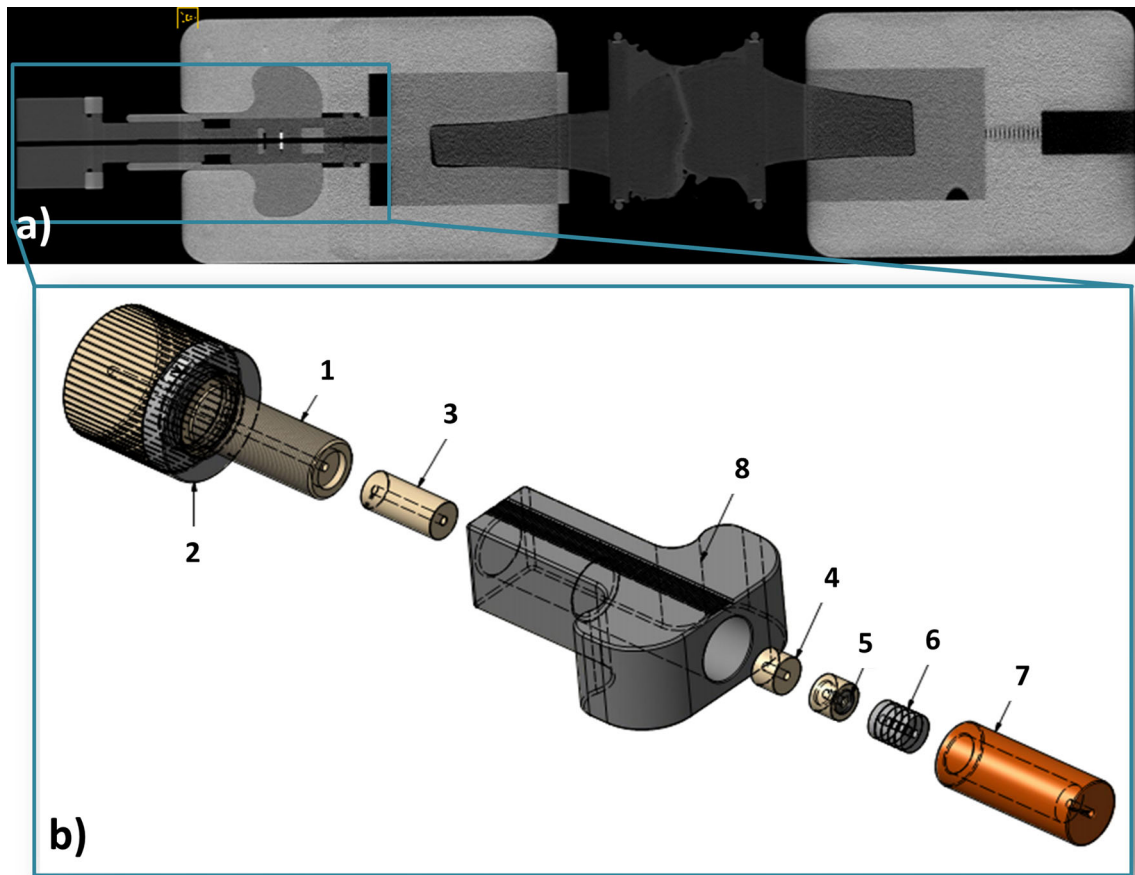


Fig. 4 **a** Axial cross-sectional CT scan of the entire compression device with the bone models in place. **b** Magnified schematic representation of the actuator on the tibial side (framed *blue* in **a**: Rotations of a PEEK screw (1) were guided by a PVC scale ring (2) and actuated an array of three PEEK bolts (3–5), five stacked pressure plates (6)

and the principal PEEK pressure bolt (7), which were contained within the main casting (8). Rotations brought about axial displacement of the tibial holding shells positioned in front of the principal pressure bolt. The configuration of the PEEK screw (1) created an axial displacement of 1 mm per 360° rotation

For the present validation, the sensor was inserted into the joint covering the femoral articular surfaces, while avoiding crinkling of the sensor and its specific position was secured using thumbtacks. Due to the sensor dimensions, only the anterior two-thirds of the femoral articular surface were covered. However, complete coverage of the area of interest was verified. Before measurements were conducted, the sensors were preconditioned, equilibrated and calibrated according to the manufacturer's instructions.

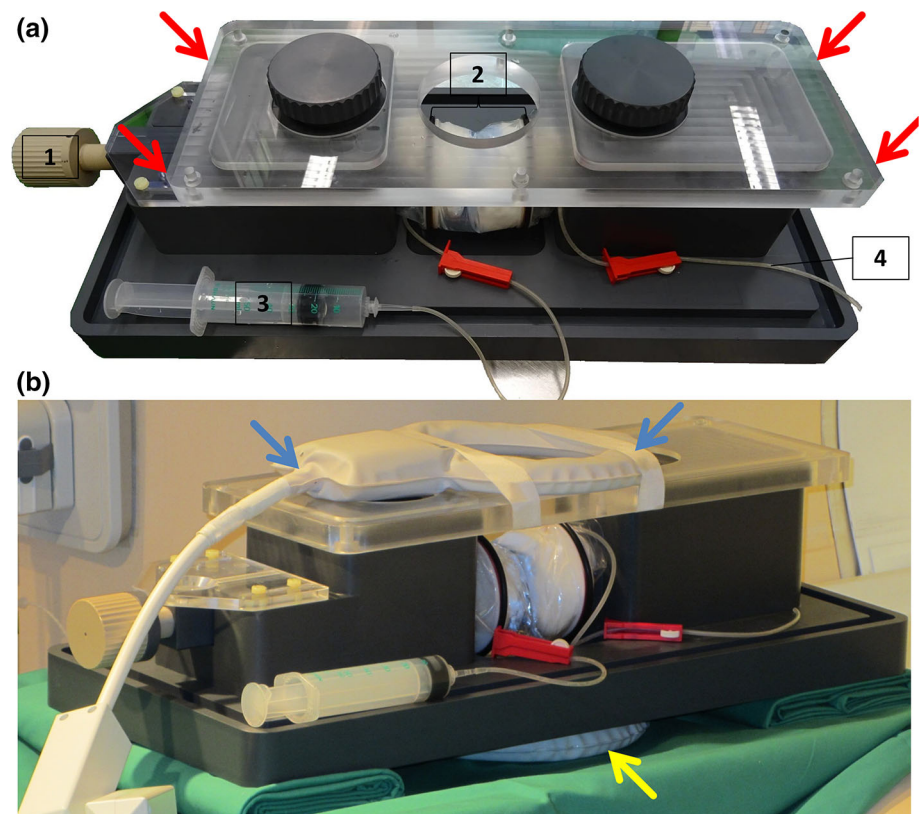
Measurements were conducted sequentially using the wiroxil[®]-coated bone models with the 8-mm-diameter defect at the centre of the medial femoral condyle (measurement series 1), using the wiroxil[®]-coated bone models upon filling of the defect with the ordinary wiroxil[®] plug (measurement series 2) and with a cartilage sample of similar thickness (measurement series 3) (see Sect. 2.3.1). Each measurement protocol was performed as follows: After determining the initial contact point (i.e. the axial displacement position with a contact area $>1 \text{ mm}^2$), further axial displacements of the

tibial component to 2.5 mm ($\delta_{2.5}$) and to 5 mm ($\delta_{5.0}$) were applied by manual actuation at a strain rate of ca. 1 mm/s. The resultant spatially resolved contact pressure (kPa) and contact area (mm^2) data were measured in real time, recorded, imported into MATLAB (MatlabR2014a, Natick, USA) and analysed using customized analysis routines.

Measurement series 1 was used to locate the defect, while measurement series 2 and 3 were used to determine the exact mean pressure levels of the cartilage sample at $\delta_{2.5}$ and $\delta_{5.0}$. Overall, similar mean pressure levels were found; for the cartilage sample and the wiroxil[®] plug, local pressures were $679.6 \pm 88.4 \text{ kPa}$ and $609.8 \pm 57.5 \text{ kPa}$ (at $\delta_{2.5}$) and 1050.6 ± 100.0 and $941.9 \pm 93.4 \text{ kPa}$ (at $\delta_{5.0}$).

Longitudinal measurements of the mean pressure levels of the cartilage sample over time were performed, too (measurement series 4). To this end, displacement was set to $\delta_{2.5}$ (and $\delta_{5.0}$, of course) and mean pressure levels were determined after 1, 2, 5, 10, 20, 30 and 45 minutes. Considerable decreases in pressure over time were found for

Fig. 5 **a, b** Whole-knee joint compression device outside **(a)** and within the bore of the 3.0T MRI system **(b)**. **a** A transparent polymethylmethacrylate cover plate (outlined by red arrows in **a**) was fitted to the non-mobile PVC components' top surfaces to compensate for any bending forces present during compressive loading [(1) screw of actuating mechanism; (2) knee model with PBS-buffer-filled joint capsule; (3) syringe with extension (for inflow regulation); (4) extension for outflow regulation]. **b** MR imaging was performed using a dual-coil set-up with the first coil attached to the upper (blue arrows) and the second coil attached to the lower surface (yellow arrow) of the compression device



$\delta_{2.5}$ (-6.7 , -14.4 , -22.9 , -28.3 , -38.1 , 41.6 , and -48.3 % after 1, 2, 5, 10, 20, 30 and 45 min), while moderate decreases were found for $\delta_{5.0}$ (-4.8 , -8.2 , -13.6 , -19.0 , -25.0 , -29.4 , and -32.8 %). These changes were significantly different [one-way ANOVA, $p < 0.001$ ($\delta_{2.5}$); $p < 0.001$ ($\delta_{5.0}$)].

2.3 In situ imaging studies

2.3.1 Preparation of cartilage samples

A total of five chondral (i.e. cartilage layer-only) samples were obtained for the response-to-loading assessment. These samples were obtained from patients undergoing total knee arthroplasty because of primary osteoarthritis [3 females; 3 left; age 65.6 ± 6.4 years (range 56–73 years)]. Upon sterile excision, the excised cartilage–bone material was collected in sterile DMEM medium containing 100 U/ml penicillin, 100 μ g/ml gentamycin and 1.25 U/ml amphotericin-B (all from Gibco-BRL, Gaithersburg, US). Only macroscopically uniformly intact samples without visible structural damage [Outerbridge grade 0 (Outerbridge 1961)] from the central part of the medial femoral condyle were included in our study. By use of an 8-mm-diameter skin biopsy punch and a #13 scalpel (both from pfm-medical), the subchondral bone was removed and cylindrical chondral samples were cut from the surgical material. A dedicated cutting

device (metal block with circular moulds of 8-mm-diameter and 3.0 mm depth) was used to obtain chondral samples of uniform thickness which was confirmed using a digital micrometry (Mitutoyo 293-521, Tokyo, Japan). After preparation, the chondral samples were placed into the 8 mm defect within the wirozil[®] layer (Fig. 2d). Special care was taken to precisely align the sample with the surrounding wirozil[®] layer en niveau and to avoid a step-off at the interface. No adhesive was used to attach the sample to the femoral bone model.

2.3.2 MR imaging studies

After sample preparations and filling of the joint capsule with standard PBS buffer, the device was centrally positioned within a clinical 3.0T scanner (Achieva, Philips, The Netherlands). Imaging was performed using a clinical standard dual-coil set-up (Sense-Flex M, Philips), which were attached to the upper and lower surfaces of the device using medical adhesive tape (Fig. 5). The coil set-up fully comprised the knee joint model in its entirety, and the centre of the articular surface of the medial femoral condyle was positioned within the centre of the coils for maximized signal-to-noise ratio. Prior to the actual measurements, MRI compatibility was tested using a series of T2*-weighted gradient echo sequences (2D sequences; coronal, sagittal, axial; parameters: TR = 653.9 ms, TE = 18.4 ms, flip angle

(FA) = 18°, 18 slices, ST = 5 mm, SG = 6 mm, FOV = 120 mm × 120 mm, AM = 256 × 205, NSA = 1). No significant b_0 inhomogeneity was found.

The response-to-loading assessment by MRI was carried out at three displacement positions: (1) unloaded (δ_0), i.e. at a distance of ca. 1 mm to the initial contact point; (2) at $\delta_{2.5}$; and (3) at $\delta_{5.0}$. In consideration of the clinical practice, proton-density-weighted (PDW) and T2-weighted sequences were acquired at these displacement positions. These sequences are most commonly applied in imaging of knee cartilage and the knee joint in general (Roemer et al. 2011). Of note, PDW imaging was therefore performed at an in-plane resolution of 0.4 × 0.53 mm, while T2-weighted imaging was performed at an in-plane resolution of 0.47 × 0.47 mm.

Absence of sample dislocation during preparation was confirmed by δ_0 measurements. While the PDW sequences were acquired in the three standard planes perpendicular to each other (i.e. sagittal, coronal and axial), the T2-weighted sequences were only acquired in the coronal plane. For the PDW sequences, the following sequence parameters were applied: repetition time (TR) 4048 ms; echo time (TE) 15 ms; slice thickness (ST) 3 mm; interslice gap (SG) 3.3 mm; 28 slices; acquisition matrix (AM) 400 × 302; number of signal averages (NSA) 1; field of view (FOV) 160 × 160 mm²; turbo factor (syn. echo train length) 14. The PDW images were used to guide the coronal imaging slice for the T2-weighted sequence to create a central bisecting slice through the sample. 2D multi-spin echo sequences using eight echo times [TE = $n * 9$ ms (n ranging from 1 to 8)] were used to determine T2 values in this slice; further parameters of the sequence were as follows: TR 1000 ms; flip angle (FA) 90°; ST 2 mm; NSA 3; acquisition matrix 64 × 64; FOV 30 × 30 mm². Upon completion of measurements at δ_0 , axial displacement to $\delta_{2.5}$ was applied, confirmed using coronal MRI scout views and an equilibration period of 5 min was observed prior to PDW and T2-weighted measurements, which took 12:48 min (PDW; cor, sag, ax) and 3:26 min (T2; cor) per displacement position and sample, respectively. Analogously, axial displacement to δ_5 and subsequent MRI measurements were performed. T2 maps were generated as before (Nebelung et al. 2016b, 2017) using customized monoexponential fitting routines provided in MATLAB R2016a software (MATLAB, Natick, MA, USA). Of note, only values with echo times ≤ 60 ms were included due to the low signal at higher echo times. Fit quality was checked using R^2 statistics adjusted to the degrees of freedom. For T2 map segmentation, sample outlines were segmented manually on the basis of the corresponding mid-coronal morphological PDW image. Due to partial volume effects, only pixels that lay safely within the cartilage were used, while boundary pixels (i.e. pixels that were not safely within the sample) were excluded. The entire sample cross section at the mid-coronal plane was defined as the region of

interest for subsequent quantitative analysis in terms of mean T2 values.

Using the inbuilt digital caliper tool of the picture archiving and communication system (PACS), the chondral sample height was determined at the respective sample centre (i.e. at 4 mm equidistance to both defect shoulders) on sagittal and coronal PD-weighted views alike. Moreover, throughout the successive displacement positions the distance between the bone model's femoral and tibial surface was measured at the sample's centre on sagittal PDW images. MR imaging was performed at room temperature, which was monitored at the beginning and the end of the acquisition period (20.3 ± 0.6 °C).

2.4 Reference evaluation

2.4.1 Biomechanical studies

After MRI measurements, cartilage samples were retrieved from the loading device, reimmersed in DMEM + additives as above and studied biomechanically. As before (Nebelung et al. 2017), a Zwick/Roell Z2.5 universal mechanical testing machine (Ulm, Germany) with a 20-mm-diameter compressive piston and a 200 N load cell was used to perform unconfined compression tests on the cylindrical chondral samples. Samples were compressed to the maximum strain of 21% at a strain rate of 0.005/s. Specific loading protocols and the resultant load sharing between the solid matrix and fluid pressurization in relation to the strain rate have been thoroughly assessed earlier (Li and Herzog 2004): At a strain rate of 0.005%/s, the extracellular matrix has been shown to bear more than 80% of the applied load. Using TestXpert software (Zwick/Roell), load and displacement data were simultaneously recorded and the ratio of stress and strain, which was defined as Young's modulus (YM), was derived by fitting a tangent to the range of 10–20% strain (Jurvelin et al. 1997; Li and Herzog 2004). During biomechanical studies, samples were kept hydrated with DMEM + additives as above.

In addition, two wirosil® plugs of 3 mm height as well as the wirosil® plug obtained upon creation of the defect were biomechanically measured using the same biomechanical set-up as detailed above.

2.4.2 Histological studies

The histological analyses were performed as described earlier (Nebelung et al. 2016b, 2017, 2016c). Briefly, cartilage–bone regions from adjacent sample regions were used for histological assessment and histological sections were prepared parallel to the MR imaging plane. Upon decalcification and fixation in Ossa fixona (Diagonal, Muenster, Germany), embedding in paraffin, cutting to 5- μ m sections and staining with haematoxylin/eosin and Safranin O according to

standard protocols, slices were imaged using a Leica microscope (DM/LM-P, Wetzlar, Germany) and visualized using Diskus software of the same manufacturer. Histological analysis included measurement of cartilage thickness and semi-quantitative histological grading of cartilage degeneration according to Mankin et al. (1971). Mean cartilage thickness was determined using the inbuilt caliper tool at three central locations at 1-mm intervals. Mankin grading was performed by three blinded investigators with experience in musculoskeletal histopathology [SN (MD, experience: 7 years, fellowship trained); HJ (PhD, experience: 15 years, fellowship trained); MP (BSc, experience: 2 years)]. Each investigator assessed the samples individually, and in case of divergent scoring, individual slices were discussed until a consensus was reached. The Mankin classification assesses structural (score 0–6), cellular (score 0–3), proteoglycan staining-associated (score 0–4) and tidemark integrity-associated tissue properties (score 0–1), which are scored separately and summed up (Mankin sum score, range 0–14); 0 indicates no histological signs of degeneration, while 14 indicates most severe signs of degeneration.

2.5 Statistical analysis

GraphPad Prism (v5.0, San Diego, USA) was used to perform statistical analyses. Mann–Whitney’s test was used for group-wise comparisons of Young’s modulus between chondral samples and wiroxil® plugs, while Wilcoxon’s signed-rank test was used to compare the stress–strain curves of cartilage and wiroxil®. One-way ANOVA was used to assess spatially resolved pressure levels as a function of time (measurement series 4). Repeated-measures ANOVA was used to detect differences between modalities (i.e. MRI, histology and micrometry) in terms of sample thickness and between T2 maps as well as between longitudinal thickness measurements by MRI (i.e. at δ_0 , $\delta_{2.5}$, and $\delta_{5.0}$).

3 Results

Close biomechanical correspondence between native cartilage and wiroxil® was confirmed by conventional biomechanical assessment. Young’s modulus was determined as 0.320 ± 0.057 MPa ($n = 3$, wiroxil® plugs) and 0.419 ± 0.143 MPa ($n = 5$, chondral samples) ($p = 0.250$, Mann–Whitney test). Detailed analysis of the two materials’ stress–strain characteristics revealed slightly disparate curves, although the overall curve morphology was similar (Fig. 6). The two curves were found to be significantly different ($p < 0.001$, Wilcoxon signed-rank test), indicating higher stiffness of native cartilage, in particular at higher strains.

Response-to-loading assessment was performed on five human articular cartilage samples. The distance between

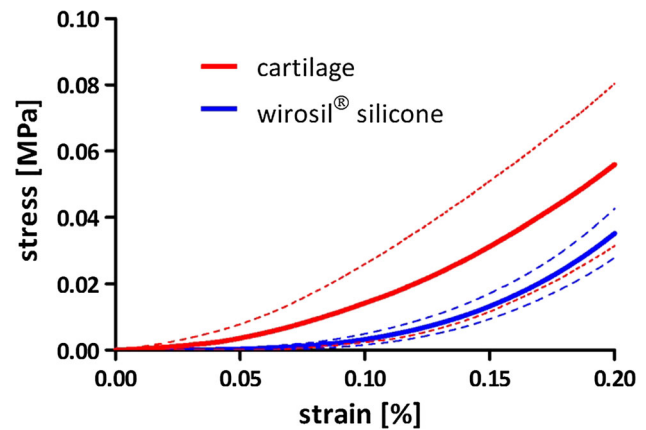


Fig. 6 Stress–strain curves determined for cartilage samples (red) and wiroxil® plugs (blue) of equal dimensions (height: 3 mm, diameter: 8 mm). Means (solid line) and standard deviations (dashed lines). Cartilage ($n = 5$), wiroxil® ($n = 3$). Unconfined compression test, maximum strain 21%, strain rate 0.005/s

the bone model’s femoral and tibial surfaces as assessed on sagittal PDW images was determined as 3.5 ± 0.2 mm ($\Delta_{0-2.5}$) and 2.5 ± 0 mm ($\Delta_{2.5-5.0}$). Baseline characteristics of these samples were similar overall. Histological evaluation revealed all samples to be grossly intact (Mankin grade 0), although the mean Mankin score sum of 1.8 ± 1.3 (range 0–3) indicated the presence early signs of degeneration in some samples (Table 1). Cartilage samples’ thickness as determined by digital micrometry, MR imaging and histology was found to be similar overall (Table 1).

At δ_0 , $\delta_{2.5}$, and $\delta_{5.0}$, all chondral samples could be visualized in their entirety by MRI. Longitudinal comparative evaluation of sample morphologies (i.e. at δ_0 vs. $\delta_{2.5}$ and $\delta_{5.0}$) revealed quantitative and qualitative changes in all samples. In quantitative terms, significant decreases in sample height were found at the consecutive loading positions [δ_0 , 2.86 ± 0.25 mm; $\delta_{2.5}$, 2.56 ± 0.25 mm; $\delta_{5.0}$, 2.02 ± 0.16 mm; $p < 0.001$ (repeated-measures ANOVA)] (Table 1), while sample circularity remained unchanged. Qualitative evaluation of sample characteristics on PDW images confirmed these findings (Fig. 7). Moreover, changes in T2 signal intensity in response to loading were noted. T2 relaxation is governed by collagen content and orientation as well as water content (Menezes et al. 2004). Therefore, loading-induced changes in T2 need to be considered in light of structural and compositional changes of hydration and of collagen orientation at the molecular level. T2 signal intensity was grossly similar irrespective of compressive loading at shorter echo times (Fig. 8a), while marked decreases in T2 signal intensity were observed at longer echo times, in particular with higher compressive loading and secondary pressurization of the tissue (Fig. 8b, c). In T2 maps, corresponding changes were noted (Fig. 8d), although these changes were not consistent in quantitative terms throughout all samples: δ_0 , 41.2 ± 4.2

Table 1 Thickness of human articular samples (mm) as determined by histology, digital micrometry, and magnetic resonance imaging (MRI) in the unloaded state (δ_0)

Sample number	Sample thickness (mm)			Reference Evaluation		
	Histology δ_0	Micrometry δ_0	MRI δ_0	$\delta_{2.5}$	Biomechanics Young's modulus (MPa)	Histology Mankin score (sum)
1	2.77	3.03	2.8	2.5	0.486	3
2	2.94	2.96	3.1	2.8	0.403	2
3	2.90	2.99	2.5	2.2	0.587	3
4	2.82	3.07	2.8	2.5	0.198	1
5	2.35	2.99	3.1	2.8	0.419	0
M \pm SD	2.76 \pm 0.24	3.01 \pm 0.04	2.86 \pm 0.25	2.56 \pm 0.25	0.419 \pm 0.143	1.80 \pm 1.30
P	0.263			p < 0.001		

Respective sample thickness as determined by MRI during compressive loading to 2.5 mm ($\delta_{2.5}$) and 5.0 mm ($\delta_{5.0}$) displacement. Statistical differences between modalities and loading positions were assessed using repeated-measures ANOVA. Significant differences are bold. For reference purposes, sample-specific biomechanical and histological data are displayed, too

ms; $\delta_{2.5}$, 43.3 \pm 1.9 ms; $\delta_{5.0}$, 40.2 \pm 2.8 ms; $p = 0.208$ (repeated-measures ANOVA); $n = 5$.

4 Discussion

The most important findings of the present study are that (1) the developed whole-knee joint compressive loading device allows for consistent, standardized and reproducible loading of human articular cartilage samples in a close-to-physiological configuration and that (2) cartilage samples undergo structural and compositional changes in response to compressive loading that may be visualized by MRI and related to histological and biomechanical tissue properties.

In efforts to provide the basis for functional cartilage assessment by MRI in a scientific context, the device's principal set-up, its MRI compatibility and the effective, quasi-static, displacement-controlled compressive loading of the cartilage samples under simultaneous MR imaging have been demonstrated. For practical reasons and with regard to the clinical requirements, samples were subjected to loading conditions amounting to around 20 and 110% of standard body weight (80 kg). Resultant stress levels experienced by the cartilage samples were determined to range between 0.7 ($\delta_{2.5}$) and 1.1 MPa ($\delta_{5.0}$), which is considered moderate and in line with earlier studies (Donahue et al. 2002; Pena et al. 2006). The applied stress level was sufficient to induce relevant morphological changes within the tissue, in particular at $\delta_{5.0}$. However, as chondrocyte viability may be adversely affected by loading outside the elastic range of cartilage deformation (Bae et al. 2007), a balance has to be struck between biomechanically sufficient loading regimes that are diagnostically beneficial on the one side and physiologically safe loading regimes that do not damage the tissue. To further refine such loading regimes, future studies should take into account post-loading cartilage viability by assessment of chondrocyte survival rates, for example by live/dead assays.

Loading-induced changes in sample morphology as assessed by MRI were noted. In quantitative terms, decreasing sample heights were found in all samples in response to loading, which is not surprising given the considerable displacement of 2.5 ($\delta_{2.5}$) and 5.0 mm ($\delta_{5.0}$). Sample width and length were not altered in response to loading, at least within the resolution limits of the sequences used (i.e. in-plane resolutions of 0.4 \times 0.53 mm/pixel for PDW images and 0.47 \times 0.47 mm/pixel for T2-weighted images). Correspondingly, morphological changes were observed in all samples in T2-weighted sequences. T2 is sensitive to the mobility of the protons within the extracellular water, which is restricted by the architectural make-up of the surrounding collagen fibres and proteoglycans and therefore commonly considered to be a marker of water content as well as collagen content and orientation in cartilage (Palmer et al. 2013). In

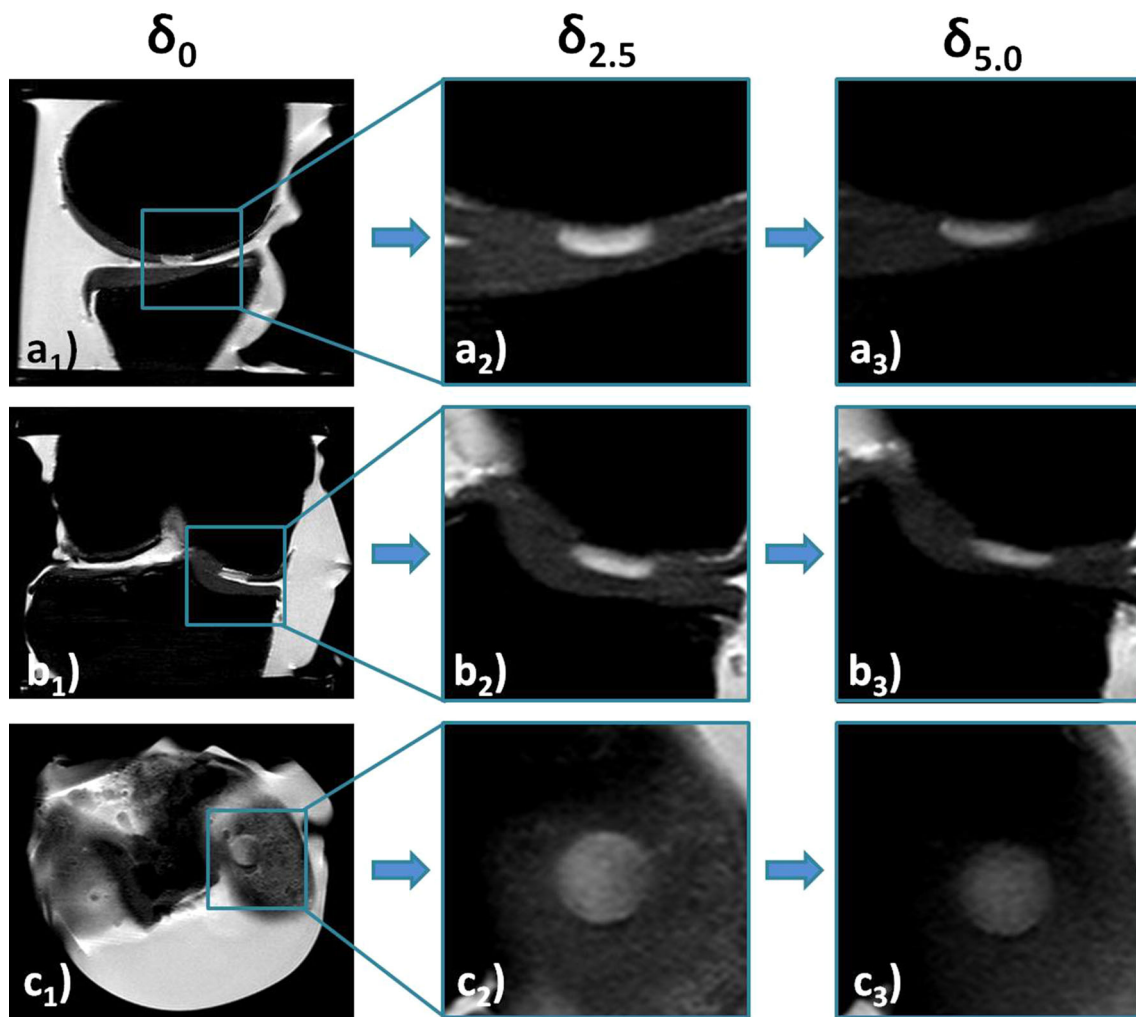


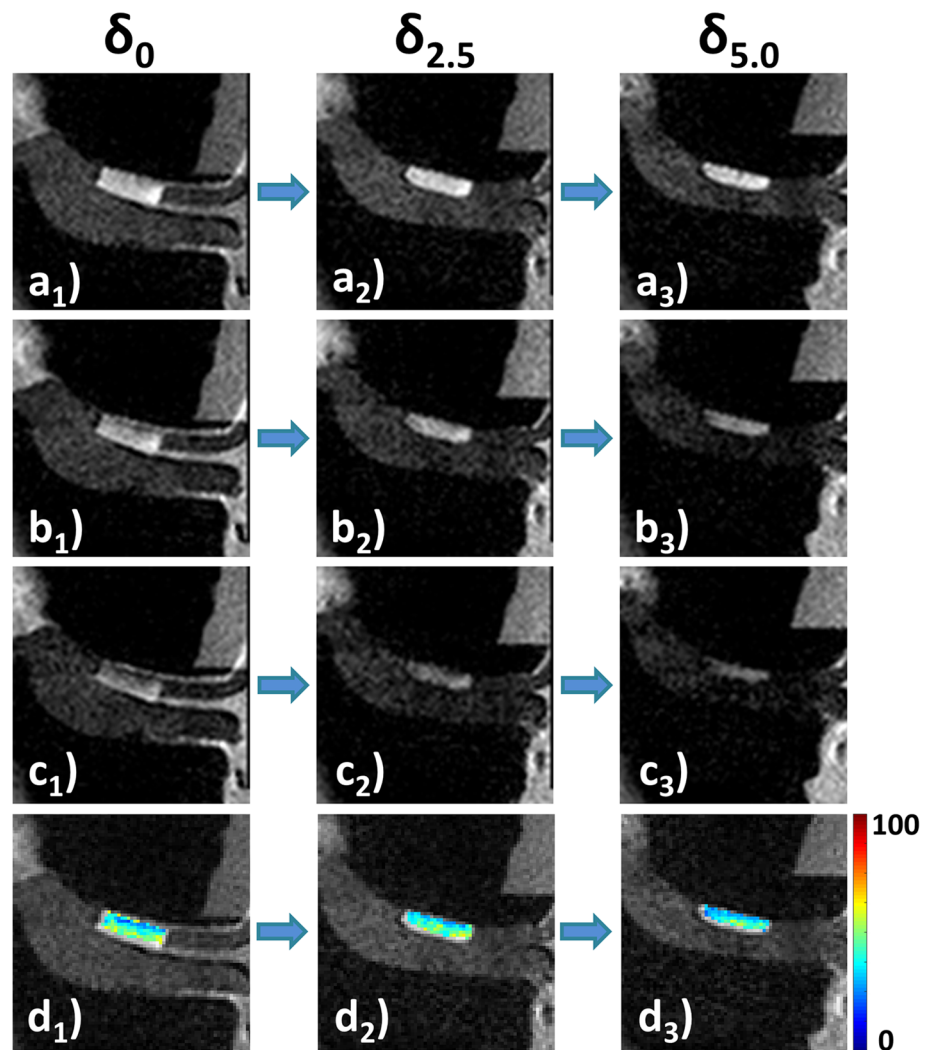
Fig. 7 Proton-density-weighted sagittal (**a**), coronal (**b**) and axial (**c**) views of the whole-knee joint loading apparatus with the wirozil[®]-coated femoral (top in **a**, **b**) and tibial (bottom in **a**, **b**) bone models at consecutive compression positions [unloaded, δ_0 (**a**₁–**c**₁); at 2.5 mm

displacement, $\delta_{2.5}$ (**a**₂–**c**₂); at 5.0 mm displacement $\delta_{5.0}$ (**a**₃–**c**₃)]. The native cartilage sample was placed within the standardized defect at the anteromedial femoral condyle [framed in *blue* (**a**₁–**c**₁) and displayed in higher magnification (**a**_{2,3}–**c**_{2,3})]

T2-weighted images, in particular those obtained at longer echo times, an accentuated decrease in T2 signal intensity was noted in response to loading. Of course, this observation is also due to the fact that less tissue volume gives less signal due to compression; however, in the context of our study, T2-hypointense (i.e. darker) areas signify changes in water content and collagen orientation due to relevant intra-tissue pressurization secondary to compressive loading. In terms of hydration, compressive loading most likely induced considerable water redistribution within and possibly out of the tissue. Molecular-level changes meanwhile are more complex: In terms of their orientation to the static magnetic field (b_0), collagen fibres demonstrate different behaviour under load. Fibres that are radially oriented tend to spread out, while fibres that are tangentially oriented tend to be flattened. As both phenomena affect T2 signal intensity (Grunder 2006),

decreases in T2 signal intensity are most likely due to substantial collagen fibre reorientation in response to loading. Even though quantitative analysis of the five samples did not reveal loading-induced changes in T2 values to be significant, qualitative evaluation of the T2 maps indicated substantial adaptive processes within the tissue. Although this observation has been made before (Juras et al. 2009; Nebelung et al. 2016a, 2017), the close-to-physiological loading mechanism offered by our set-up has to be considered at this point. Physiologically, articular cartilage experiences a combination of compression and shearing alike when bearing load. A recent in-vivo study investigating the loading-induced changes in cartilage by MRI demonstrated pure shear to be the dominant loading mode and more relevant to subsequent cartilage deformation than axial compression (Chan et al. 2016). This is likely due to the tissue's relative compliance

Fig. 8 T2-weighted coronal images of the cartilage sample within the knee joint loading apparatus obtained at increasing echo times [9.01 ms (a), 27.04 ms (b), 45.06 (c)] and resultant T2 maps [d (ms)]. Consecutive compression positions [i.e. unloaded, δ_0 (a₁–d₁); at 2.5 mm displacement, $\delta_{2.5}$ (a₂–d₂); at 5.0 mm displacement $\delta_{5.0}$ (a₃–d₃)]. Figure legend and sample as in



yet incompressibility, which brings about considerable lateral displacement. As the expansion is limited by the stiff underlying subchondral bone (in vivo) and the thermoplastic bone model (in our set-up), high shear stresses throughout the tissue develop and are certain to contribute to the intra-tissue pressurization. Therefore, experimental loading protocols applying indentation as before (Juras et al. 2009) may not adequately reflect the actual in-vivo process of load bearing and underline the need for physiological and close-to-physiological experimental set-ups.

No significant differences between samples in their specific response-to-loading were found as the cartilage samples were relatively homogeneous as determined by histological and biomechanical measures. Histologically, all samples were graded as ‘intact’ based on the classification of Gahunia et al. (1995), although some samples exhibited signs of early degeneration which is not surprising given the tissue source of total knee replacements. Correspondingly, even though some biological variability was found, Young’s modulus was grossly similar in all cartilage samples, too.

However, future studies should take more complex biomechanical evaluation protocols to determine equilibrium properties into consideration in efforts to more comprehensively assess cartilage biomechanics. Of course, larger sample sizes need to be investigated to determine the exact contribution of the biological factors to the sample’s response to loading.

Wirosil[®] silicone (polyvinyl siloxane) was used as a cartilage-mimicking material to create close-to-physiological loading conditions. Wirosil[®] has been used in comparable studies (Lopez et al. 2007) due to its artefact-free MRI signal, easy preparation, mechanical stability and high stiffness. In terms of Young’s modulus no significant differences between cartilage samples and wirosil[®] plugs were found; however, further in-depth analysis of the stress–strain curves indicated distinct differences between both materials. Although an overall similar stress response was noted, native cartilage is stiffer than wirosil[®], in particular at higher strains, which indicates that our experimental set-up is not entirely physiological.

The wirosil[®] stress–strain characteristics, in particular its stress relaxation, need to be considered when mid-to-long-term uniaxial quasi-static loading and longer MRI measurement protocols are applied, for example in the context of quantitative MRI measurements such as T1 ρ or T2* mapping that assess different extracellular matrix components (Nebelung et al. 2016b, 2017; Palmer et al. 2013). Hence, longitudinal changes of effective mean stress levels experienced by the cartilage samples were studied. Mean stress levels were found to be considerably decreased over time at $\delta_{2.5}$, while they were found to be moderately decreased at $\delta_{5.0}$. Here, basic biomechanical principles of the cartilage sample itself and of wirosil[®] as the articulating joint partner need to be considered. Polyvinyl siloxane (which is the chemical substance commercially available as wirosil[®]) is theorized to not display considerable stress relaxation due to high dimensional stability (Mandikos 1998). The physiological stress relaxation response of cartilage, however, is associated with fluid redistribution secondary to loading until the compressive stress is matched by the equilibrium stress determined by the solid matrix (Li and Herzog 2004). Upon loading, stress relaxation occurs rapidly in cartilage and mean stress levels are levelling off to the equilibrium stress levels in the mid-to-long term, which may help explain the considerably higher decreases in mean stress levels at $\delta_{2.5}$ in contrast to the more moderate decreases at $\delta_{5.0}$. Although complete equilibrium may not be reached for hours if high compressive loads are applied to the tissue (Myers and Mow 1983), the considerable stress relaxation of the articulating joint partners (i.e. native cartilage and wirosil[®]) needs to be considered when biomechanical parameters are related to MRI-derived parameters assessing the response to loading. Future in situ loading approaches may make use of a pressure-controlled loading configuration to achieve more consistent mid-to-long-term compressive loading.

Displacement-controlled compressive loading was generated along the mechanical axis of the leg. Bone-to-bone measurements on sagittal PDW images between the bone model's femoral and tibial surfaces revealed consistent displacement of the bone models towards each other in the presence of native cartilage at the defect site. Therefore, the compressive loading device is sufficiently incompressible to consistently and reproducibly apply the above-mentioned loads, despite being made of plastic. The possibility of substantial deformation of the device's materials during loading can therefore be excluded. Although the cartilage samples conformed well to the specific anatomy of the medial femoral condyle due to their similar topographic origin, the rigid set-up precluded any motion other than along the mechanical axis of the leg. However, load bearing of the native knee involves more complex processes as has been demonstrated in a number of classical studies (Ahmed and Burke 1983; Kurosawa et al. 1980). While the knee joint is not congru-

ous at lower loads, it becomes markedly more congruous at higher loads and the area of contact is gradually widened to involve both compartments' central and peripheral areas. This is the result of conforming motions of the tibia to the femur during knee extension, which involves external rotation of the tibia and is due to the asymmetry of the femoral condyles (commonly called the 'screw-home' mechanism). Moreover, menisci and internal ligaments were not included in our set-up. This is particularly relevant for the menisci as these structures provide surface compliance, transmit stresses across wider areas of the joint and, therefore, help to avoid excessive stresses within the articular cartilage (Kurosawa et al. 1980). A meniscus-deficient knee being subject to compressive loading experiences considerable decreases in contact area size and, consequentially, increases in mean stress levels (Ahmed and Burke 1983; Kurosawa et al. 1980). Our set-up did not take these joint specific aspects into consideration and, therefore, its realization of true physiology is limited.

These issues may be addressed by cadaver studies. However, it is important to note that even though chondrocytes are resistant to hypoxia as well as nutritional deficits and have been shown to remain viable during the early postmortem period, human articular cartilage undergoes postmortem degradation as a function of time and storage conditions (Alibegovic et al. 2014). Moreover, in particular with regard to the standardized intra-sample referencing towards histology and biomechanics our set-up may be advantageous as it allows for facilitated post-measurement sample retrieval. However, for cadaver cartilage as well as for total knee replacement cartilage, it remains unclear whether and to what extent the ex vivo MRI measurements are reflective of the actual in-vivo situation. In terms of quantitative MRI parameters, we are not aware of any study that demonstrates correlation of pre- and postoperative MRI relaxation measures.

5 Conclusions

We developed a whole-knee joint in situ compressive loading device to noninvasively assess the response to loading of human articular cartilage by MRI in terms of structure and function as well as in relation to its histological and biomechanical properties. This set-up provides a close-to-physiological experimental setting for further in-depth evaluation of the functional properties of cartilage using quantitative and qualitative MRI parameters as a measure of loading-induced intra-tissue changes. Thus, cartilage may be functionally evaluated beyond mere static analysis with promising perspectives in the more refined assessment of its pathologies.

Acknowledgements The authors would like to thank Mr. Axel Honné and the entire team of the Scientific Workshop of the University Hospital Aachen, Germany, for their invaluable support throughout this project. Furthermore, they would like to thank Ms. Sophie Lecoururier for performing the histological workup and Mr. Simon Oehrl for helping with the MRI measurements. This study was supported by the START-Program of the Faculty of Medicine, RWTH Aachen, Germany (691702, 691551). HJ is a member of the D-BOARD consortium. The D-BOARD project has received funding from the European Union's Seventh Framework Programme for Research, Technological Development, and Demonstration under Grant Agreement No. 305815. Furthermore, the authors do not have any financial, consulting or personal relationships with other people or organizations to disclose. The funding sources had no involvement in the conduct of the research or preparation of the article, in the study design, in the collection, analysis and interpretation of the data, in the writing of the report or in the decision to submit the article for publication. All authors have approved the final version of the article to be submitted.

References

- Agneskirchner JD, Hurschler C, Wrann CD, Lobenhoffer P (2007) The effects of valgus medial opening wedge high tibial osteotomy on articular cartilage pressure of the knee: a biomechanical study. *Arthroscopy* 23:852–861. doi:10.1016/j.arthro.2007.05.018
- Ahmed AM, Burke DL (1983) In-vitro measurement of static pressure distribution in synovial joints-part I: tibial surface of the knee. *J Biomech Eng* 105:216–225
- Alibegovic A, Balazic J, Petrovic D, Hribar G, Blagus R, Drobnic M (2014) Viability of human articular chondrocytes harvested post-mortem: changes with time and temperature of in vitro culture conditions. *J Forensic Sci* 59:522–528. doi:10.1111/1556-4029.12330
- Andriacchi TP, Koo S, Scanlan SF (2009) Gait mechanics influence healthy cartilage morphology and osteoarthritis of the knee. *J Bone Joint Surg Am* 91(Suppl 1):95–101. doi:10.2106/JBJS.H.01408
- Bae WC, Schumacher BL, Sah RL (2007) Indentation probing of human articular cartilage: effect on chondrocyte viability. *Osteoarthr Cartil* 15:9–18. doi:10.1016/j.joca.2006.06.007
- Bay-Jensen AC et al (2010) Which elements are involved in reversible and irreversible cartilage degradation in osteoarthritis? *Rheumatol Int* 30:435–442. doi:10.1007/s00296-009-1183-1
- Chan DD, Neu CP, Hull ML (2009) Articular cartilage deformation determined in an intact tibiofemoral joint by displacement-encoded imaging Magnetic resonance in medicine. *Magn Reson Med* 61:989–993. doi:10.1002/mrm.21927
- Chan DD, Cai L, Butz KD, Trippel SB, Nauman EA, Neu CP (2016) In vivo articular cartilage deformation: noninvasive quantification of intratissue strain during joint contact in the human knee. *Sci Rep* 6:19220. doi:10.1038/srep19220
- Donahue TL, Hull ML, Rashid MM, Jacobs CR (2002) A finite element model of the human knee joint for the study of tibio-femoral contact. *J Biomech Eng* 124:273–280
- Gahunia HK, Lemaire C, Babyn PS, Cross AR, Kessler MJ, Pritzker KP (1995) Osteoarthritis in rhesus macaque knee joint: quantitative magnetic resonance imaging tissue characterization of articular cartilage. *J Rheumatol* 22:1747–1756
- Grunder W (2006) MRI assessment of cartilage ultrastructure. *NMR Biomed* 19:855–876. doi:10.1002/nbm.1092
- Guermazi A, Alizai H, Crema MD, Trattnig S, Regatte RR, Roemer FW (2015) Compositional MRI techniques for evaluation of cartilage degeneration in osteoarthritis. *Osteoarthr Cartil* 23:1639–1653. doi:10.1016/j.joca.2015.05.026
- Herberhold C et al (1999) In situ measurement of articular cartilage deformation in intact femoropatellar joints under static loading. *J Biomech* 32:1287–1295
- Johnson VL, Giuffre BM, Hunter DJ (2012) Osteoarthritis: what does imaging tell us about its etiology? *Semin Musculoskelet Radiol* 16:410–418. doi:10.1055/s-0032-1329894
- Juras V et al (2009) In vitro determination of biomechanical properties of human articular cartilage in osteoarthritis using multiparametric MRI. *J Magn Reson* 197:40–47. doi:10.1016/j.jmr.2008.11.019
- Jurvelin JS, Buschmann MD, Hunziker EB (1997) Optical and mechanical determination of Poisson's ratio of adult bovine humeral articular cartilage. *J Biomech* 30:235–241
- Kleemann RU, Krockner D, Cedraro A, Tuischer J, Duda GN (2005) Altered cartilage mechanics and histology in knee osteoarthritis: relation to clinical assessment (ICRS Grade). *Osteoarthr Cartil* 13:958–963. doi:10.1016/j.joca.2005.06.008
- Kurosawa H, Fukubayashi T, Nakajima H (1980) Load-bearing mode of the knee joint: physical behavior of the knee joint with or without menisci. *Clin Orthop Relat Res* 149:283–290
- Lee SJ et al (2006) Tibiofemoral contact mechanics after serial medial meniscectomies in the human cadaveric knee. *Am J Sports Med* 34:1334–1344. doi:10.1177/0363546506286786
- Li LP, Herzog W (2004) Strain-rate dependence of cartilage stiffness in unconfined compression: the role of fibril reinforcement versus tissue volume change in fluid pressurization. *J Biomech* 37:375–382
- Link TM, Neumann J, Li X (2016) Prestructural cartilage assessment using MRI. *J Magn Reson Imaging JMRI*. doi:10.1002/jmri.25554
- Lopez O, Amrami KK, Manduca A, Rossman PJ, Ehman RL (2007) Developments in dynamic MR elastography for in vitro biomechanical assessment of hyaline cartilage under high-frequency cyclical shear. *J Magn Reson Imaging JMRI* 25:310–320. doi:10.1002/jmri.20857
- Madry H et al (2016) Early osteoarthritis of the knee. *Knee Surg Sports Traumatol Arthrosc* 24:1753–1762. doi:10.1007/s00167-016-4068-3
- Mandikos MN (1998) Polyvinyl siloxane impression materials: an update on clinical use. *Aust Dent J* 43:428–434
- Mankin HJ, Dorfman H, Lippiello L, Zarins A (1971) Biochemical and metabolic abnormalities in articular cartilage from osteoarthritic human hips. II. Correlation of morphology with biochemical and metabolic data. *J Bone Joint Surg Am* 53:523–537
- Menezes NM, Gray ML, Hartke JR, Burstein D (2004) T2 and T1rho MRI in articular cartilage systems magnetic resonance in medicine. *Magn Reson Med* 51:503–509. doi:10.1002/mrm.10710
- Myers ER, Mow VC (1983) Biomechanics of cartilage and its response to biomechanical stimuli. In: Hall BK (ed) *Cartilage—structure, function and biochemistry*, vol 1. Academic Press, New York, pp 313–337
- Nebelung S et al (2016a) Towards optical coherence tomography-based elastographic evaluation of human cartilage. *J Mech Behav Biomed Mater* 56:106–119. doi:10.1016/j.jmbbm.2015.11.025
- Nebelung S, Brill N, Tingart M, Pufe T, Kuhl C, Jahr H, Truhn D (2016b) Quantitative OCT and MRI biomarkers for the differentiation of cartilage degeneration. *Skelet Radiol* 45:505–516. doi:10.1007/s00256-016-2334-6
- Nebelung S, Tingart M, Pufe T, Kuhl C, Jahr H, Truhn D (2016c) Ex vivo quantitative multiparametric MRI mapping of human meniscus degeneration. *Skelet Radiol* 45:1649–1660. doi:10.1007/s00256-016-2480-x
- Nebelung S et al (2017) Functional MR imaging mapping of human articular cartilage response to loading. *Radiology* 282:464–474. doi:10.1148/radiol.2016160053

- Outerbridge RE (1961) The etiology of chondromalacia patellae. *J Bone Joint Surg Br* 43-B:752–757
- Palmer AJ et al (2013) Non-invasive imaging of cartilage in early osteoarthritis. *Bone Jt J* 95-B:738–746. doi:[10.1302/0301-620X.95B6.31414](https://doi.org/10.1302/0301-620X.95B6.31414)
- Pena E, Calvo B, Martinez MA, Doblare M (2006) A three-dimensional finite element analysis of the combined behavior of ligaments and menisci in the healthy human knee joint. *J Biomech* 39:1686–1701. doi:[10.1016/j.jbiomech.2005.04.030](https://doi.org/10.1016/j.jbiomech.2005.04.030)
- Roemer FW, Crema MD, Trattng S, Guermazi A (2011) Advances in imaging of osteoarthritis and cartilage. *Radiology* 260:332–354. doi:[10.1148/radiol.11101359](https://doi.org/10.1148/radiol.11101359)
- Shiomi T et al (2010) Loading and knee alignment have significant influence on cartilage MRI T2 in porcine knee joints. *Osteoarth Cartil* 18:902–908. doi:[10.1016/j.joca.2010.05.002](https://doi.org/10.1016/j.joca.2010.05.002)
- Simonsen KP, Rasmussen AR, Mathisen P, Petersen H, Borup F (2011) A fast preparation of skeletal materials using enzyme maceration. *J Forens Sci* 56:480–484. doi:[10.1111/j.1556-4029.2010.01668.x](https://doi.org/10.1111/j.1556-4029.2010.01668.x)
- Souza RB et al (2014) Response of knee cartilage T1rho and T2 relaxation times to in vivo mechanical loading in individuals with and without knee osteoarthritis. *Osteoarth Cartil* 22:1367–1376. doi:[10.1016/j.joca.2014.04.017](https://doi.org/10.1016/j.joca.2014.04.017)
- Suero EM et al (2015) The effect of distal tibial rotation during high tibial osteotomy on the contact pressures in the knee and ankle joints. *Knee Surg Sports Traumatol Arthrosc.* doi:[10.1007/s00167-015-3553-4](https://doi.org/10.1007/s00167-015-3553-4)
- Temple-Wong MM et al (2009) Biomechanical, structural, and biochemical indices of degenerative and osteoarthritic deterioration of adult human articular cartilage of the femoral condyle. *Osteoarth Cartil* 17:1469–1476. doi:[10.1016/j.joca.2009.04.017](https://doi.org/10.1016/j.joca.2009.04.017)
- Wang H, Koff MF, Potter HG, Warren RF, Rodeo SA, Maher SA (2015) An MRI-compatible loading device to assess knee joint cartilage deformation: effect of preloading and inter-test repeatability. *J Biomech* 48:2934–2940. doi:[10.1016/j.jbiomech.2015.08.006](https://doi.org/10.1016/j.jbiomech.2015.08.006)
- Xia Y, Wang N, Lee J, Badar F (2011) Strain-dependent T1 relaxation profiles in articular cartilage by MRI at microscopic resolutions magnetic resonance in medicine. *Magn Reson Med* 65:1733–1737. doi:[10.1002/mrm.22933](https://doi.org/10.1002/mrm.22933)